PAPER

Thermal behavior of nitrocellulose-based superthermites: effects of nano-Fe₂O₃ with three morphologies†

Ting Zhang,[a] Ningning Zhao,[a] Jiachen Li,[a] Hujun Gong,[b] Ting An,[c] Fengqi Zhao[c] and Haixia Ma [ID] *[a]

Superthermites or metastable intermolecular composites (MIC) are well-known for their excellent combustion characteristics in propellants. Herein, superthermites with three Fe_2O_3 morphologies (rod-like, polyhedral, and olivary) were synthesized. The effects of Al/Fe_2O_3 on the thermal decomposition property of nitrocellulose (NC) were investigated in detail *via* differential scanning calorimetry (DSC). The results indicate that the catalytic performances of the superthermites are highly relevant to the specific surface area of their corresponding Fe_2O_3. Al/Fe_2O_3 containing rod-like Fe_2O_3 (Fe_2O_3(r)) shows a much improved performance compared with other morphological samples. The values of apparent activation energy (E_a) and thermal ignition temperature (T_{beo}) of NC-Al/Fe_2O_3(r) were the lowest. This study could provide some directive reference data for the thermal behavior of nitrocellulose-based superthermites.

1. Introduction

Metal-based nano-energetic materials (nEMs) composed of metal fuel and oxidizer are frequently referred to as superthermites or metastable intermolecular composites (MIC),[1] which are used as combustion catalysts owing to their enhanced burning rate,[2,3] short ignition lag time,[3,4] high energy release,[5] and combustion temperature.[6,7] To date, great efforts have been focused on the fabrication of various superthermites such as Al/Bi_2O_3,[8] Al/CuO,[9,10] Al/Fe_2O_3,[11] Al/I_2O_5,[12] Al/MoO_3,[13] and Al/Co_3O_4.[14] Among them, Al/Fe_2O_3, as one of the traditional thermites, is widely used as an additive in propellants, high-energetic explosives, free-standing heat sources, airbag ignition materials, hardware destruction devices, and welding torches.[15,16] The diffusion distance, contact sites, and morphology are key factors for the reactive properties of thermites. To date, many methods such as electrospinning nanofibers,[17] electrophoretic deposition,[18] ultrasonic mixing,[19] and sol–gel method[20] or atomic layer deposition (ALD) technique[21] have been applied to make the interfacial contact area of the thermites maximal. However, most of these focus on the thermite itself. In propellant systems, thermites are always

used with other components. Thus, it is necessary to study the thermal behavior of nitrocellulose-based superthermites composites.

Nitrocellulose (NC) is well known as an important ingredient in guns, explosives, and propellant formulations.[22,23] The combustion performance is the core of propulsion technology, which can be significantly improved with the help of burning catalysts. An *et al.* studied the catalytic effects of three different types of thermites on the combustion of double-base (DB) propellants. The results indicated that DB propellants containing three thermites Al/PbO, Al/CuO, and Al/Bi_2O_3 showed excellent combustion performances.[24] Yan *et al.* studied the catalytic action of nitrocellulose nanofiber-based thermite textiles compared with that of pure NC and nanoaluminum (n-Al)-incorporated nanofiber, which showed enhanced burning rates with the addition of Al/CuO composites.[17] Li *et al.* investigated the impact of Al/Fe_2O_3 on the thermal properties and elastic modulus of NC fiber. The Al/Fe_2O_3/NC fibers showed a broader exothermic peak than pure NC and the elastic modulus was improved distinctly by the addition of 5.0 wt% Al/Fe_2O_3.[25] Although there have been many efforts in this field, studies on the thermal behavior of nitrocellulose-based superthermites have rarely been reported. Therefore, the main objective of this article is to fully discuss the differences of three superthermites Al/Fe_2O_3 including their structures, profound effects on the decomposition processes of NC and catalysis action.

In this work, we design and prepare controllable NC-Al/Fe_2O_3 composites using various morphologies of Fe_2O_3. The thermal behaviours, kinetic equation of the exothermic decomposition reaction, thermal parameters and thermal safety of the NC-Al/

[a]School of Chemical Engineering, Northwest University, Xi'an 710069, Shaanxi, China. E-mail: mahx@nwu.edu.cn

[b]State Key Laboratory of Continental Dynamics, Northwest University, Xi'an 710069, Shaanxi, China

[c]Science and Technology on Combustion and Explosion Laboratory, Xi'an Modern Chemistry Research Institute, Xi'an 710065, Shaanxi, China

Fe_2O_3 hybrids are carefully studied by means of differential scanning calorimetry (DSC). We find that the different morphologies cause an extensive change in the specific surface area of the composites, which thus affects their actual catalytic action and thermal decomposition characteristics of NC. The apparent activation energy (E_a) of NC-Al/Fe_2O_3(r) decreases the most by 24.95 kJ mol^{-1} in comparison with pure NC, which reveals that Al/Fe_2O_3(r) has the best catalytic effect, thus making it a potential material for application in micro-propellants.

2. Experimental

2.1 Synthesis of nanosized Fe_2O_3

Olivary nano-Fe_2O_3. $FeCl_3 \cdot 6H_2O$ (1.0 g), NH_4HCO_3 (0.5 g), PEG (0.5 g), and 30 mL distilled water were added to a Teflon-lined stainless-steel autoclave with stirring, and then heated at 120 °C for 12 h. Subsequently, the product was washed several times with distilled water and ethanol alternately, and then dried at 60 °C. The resulting powder was Fe_2O_3 nanoparticles, which were denoted as Fe_2O_3(o).

Polyhedral nano-Fe_2O_3. Polyhedral Fe_2O_3 was synthesized according to our previous method.[26] Briefly, $K_4Fe(CN)_6 \cdot 3H_2O$ (0.24 g), CMC (1.25 g L^{-1}, 30 mL), PVPK30 (0.40 g) and $N_2H_4 \cdot 3H_2O$ (0.40 mL) were added successively to a Teflon-lined stainless steel autoclave, then the autoclave was maintained at 200 °C for 6 h and allowed to cool to room temperature. The red precipitate was collected and washed with distilled water and ethanol several times. The product was denoted as Fe_2O_3(p).

Rod-like nano-Fe_2O_3. $FeCl_3 \cdot 6H_2O$ (1 g) and NaOH (0.5 g) were mixed in 30 mL distilled water with stirring, then transferred into a Teflon-lined stainless-steel autoclave and heated at 180 °C for 6 h. Subsequently, the precipitate was washed several times with distilled water and ethanol alternately to remove possible impurities or excess ions, and then dried at 60 °C in air. The product was denoted as Fe_2O_3(r).

2.2 Preparation of Al/Fe_2O_3

Al/Fe_2O_3 superthermites were prepared via ultrasonic dispersion in n-hexane with a stoichiometric ratio of Fe_2O_3 : Al (71.1 wt% : 28.9 wt%). First, n-Al and nano-Fe_2O_3 were each dispersed using ultrasonic waves for 0.5 h. Second, the homogeneous distributions of nano-Fe_2O_3 and n-Al were put into the same reaction vessel which was placed in an ultrasonic bath and heated at 40 °C for 2 h under a nitrogen atmosphere. Finally, the sample was ultrasonically mixed until the dispersant (n-hexane) almost completely evaporated and dried at 60 °C for 6 h to obtain the final composite.

2.3 Preparation of NC-based Al/Fe_2O_3

The solid propellants with 3–5 wt% catalyst show a great effect on the burning rate,[27] therefore, physical mixtures of three types of Al/Fe_2O_3 powders and NC were prepared in an agate mortar with the mass ratio of 1 : 19 and slowly ground. The slow grinding process was maintained for 30 min to obtain the composite materials.

2.4 Characterization

The physical phase, composition, morphology and structure of the materials were characterized via XRD, SEM-EDS, TEM, FT-IR and XPS. X-ray diffractograms were recorded on a D/MAX-3C (Japan) instrument using Cu $K\alpha_1$ radiation (λ = 0.15406 nm) at 40 kV voltage and 40 mA current ranging from 10° to 80°. SEM observations were carried out on a Quanta 400 FE-SEM (FEI Co., USA) at an acceleration voltage of 30 kV. EDS spectra were measured using an INCAIE350 testing device from OXFORD Instruments INC (UK) with a discharge voltage of 4–10 kV and distance of exactly 1 mm between the electrodes. The morphology and size of the as-obtained products were investigated via transmission electron microscopy (TEM) and high-resolution transmission electron microscopy (HRTEM) on a Libra 200FE (Carl Zeiss SMT Pte Ltd., Germany). Fourier transform infrared spectroscopy (FT-IR, Bruker Tensor 27, powders were diluted in KBr) was used to investigate the nanoparticles (NPs). X-ray photoelectron spectroscopy (XPS) measurements were performed using a Thermo Scientific X-ray photoelectron spectrometer.

The BET specific surface area and pore volume of the powders were measured on an Autosorb-1C-TCD physical adsorption instrument (American Quantachrome Co.). All samples were degassed at 180 °C prior to the nitrogen adsorption measurements. The BET surface area was determined via a multipoint BET method using the adsorption data in the relative pressure (P/P_0, P_0 is the pressure of saturated nitrogen vapor at a temperature of 77.35 K) range of 0.05–1.00. Desorption isotherms were used to determine the pore size distribution via the Barrett–Joyner–Halenda (BJH) method, assuming a cylindrical pore model. The nitrogen adsorption volume at the relative pressure (P/P_0) of 0.99 was used to determine the pore volume and average pore size.

Raman spectroscopy on the three Fe_2O_3 samples was performed on a Renishaw Raman System (Renishaw Inc., model RM2000) with a red laser at 785 nm as the excitation source. The integration time for each Raman measurement was 30 s.

The thermal behaviors of the samples were determined using differential scanning calorimetry (DSC) at a heating rate of 10 °C min^{-1} from room temperature to 350 °C in an N_2 atmosphere at a flow rate of 50 mL min^{-1} under ambient atmospheric pressure. To explore the reaction mechanism of the intense exothermic decomposition processes of the NC-based superthermites and obtain the corresponding kinetic parameters [apparent activation energy (E_a) and pre-exponential constant (A)] and the most probable kinetic model function, the DSC curves at the heating rates of 5.0, 10.0, 15.0, 20.0, 25.0 and 30.0 °C min^{-1} were processed mathematically.

3. Results and discussion

3.1 Morphology analysis

The resulting sample was firstly examined by TEM, as shown in Fig. 1. The cross-sectional TEM image clearly shows a rod-like shape in Fig. 1a. Fig. 1d (the area marked white pane and the corresponding insert) shows the typical HRTEM image of the
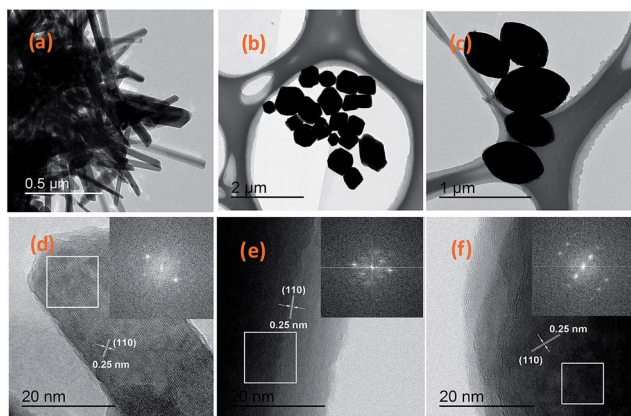
Fig. 1 TEM and HRTEM images of Fe_2O_3 with three morphologies. (a, d) $Fe_2O_3(r)$; (b, e) $Fe_2O_3(p)$; and (c, f) $Fe_2O_3(o)$. Insets: the corresponding FFT patterns marked in the white pane.

small part of an Fe_2O_3 nanorod, where only one set of clear lattice fringes with the interplanar distance of 0.25 nm could be seen, which can be indexed to the (110) plane of the rhombohedral Fe_2O_3 structure. Excellent crystallinity is also confirmed by the corresponding fast Fourier-transform (FFT) (insert in Fig. 1d). The low-magnification TEM image (Fig. 1b) of the Fe_2O_3 nanoparticles indicates that the particles have a typical polyhedral geometrical structure. From TEM image (Fig. 1c), it can be seen that the Fe_2O_3 nanoparticles are olivary in shape. The typical HRTEM images of the polyhedral and olivary Fe_2O_3 are presented in Fig. 1e and f, respectively. Both of them show almost the same crystallographic orientation with the lattice inter-planar spacing of 0.25 nm, which can be indexed to the (110) plane of the rhombohedral Fe_2O_3 structure, and is additional evidence that the nanoparticles are highly crystalline according to their corresponding FFT patterns (insert in Fig. 1e and f, respectively).

The SEM image in Fig. 2a shows Al/Fe_2O_3 nanorods with different lengths which could be due to the ultrasonic treatment. There are certain interfacial contacts between n-Al and $Fe_2O_3(r)$ in the physical mixture. The SEM images of $Al/Fe_2O_3(p)$ and $Al/Fe_2O_3(o)$ are shown in Fig. 2b and c, respectively. In these images, loosemetallized agglomerations are clearly observed. Fig. 3 shows the structures and shapes of the NC-Al/Fe_2O_3 composite materials, in which Al/Fe_2O_3 is dispersed on the surface of NC.

3.2 Structure and composition

Elemental analysis reveals that Fe, O, and Al elements are present in the Al/Fe_2O_3 superthermites. The EDS spectra of NC-Al/Fe_2O_3 confirm a distinct mixture of superthermites and nitrocellulose fibers. Fig. 4 displays the typical XRD patterns of the three types of superthermites Al/Fe_2O_3. The obvious and sharp reflection peaks of pure aluminum and iron oxide phases are in accordance with that given in the Joint Committee on Powder Diffraction Standards (JCPDS) cards 65-2869 and 33-0664, respectively. There are no unknown crystalline phases and impurities in the Al/Fe_2O_3 superthermites.

FT-IR studies (shown in Fig. 5) on the obtained superthermites were performed to ascertain their nature. For $Al/Fe_2O_3(o)$, the bands at 480 and 579 cm^{-1} are attributed to the metal–oxygen stretching vibrational mode. The Fe–O bonding bending vibration is observed at 1039 cm^{-1}. The bonding in the region of 1670–1600 cm^{-1} is ascribed to the O–H bonding bending vibrational modes. The general range of 3600–3100 cm^{-1} may be assigned to the O–H bonding stretching vibrational modes for water of hydration. A similar absorption was
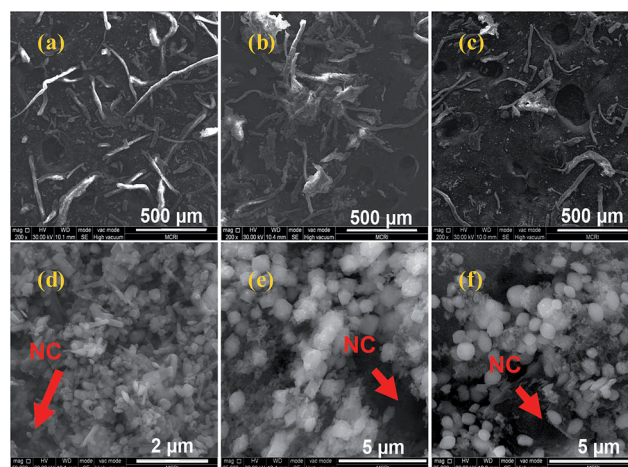

Fig. 3 SEM images of NC-Al/Fe_2O_3 (×200 magnification and ×50 000 magnification). (a, d) NC-$Al/Fe_2O_3(r)$; (b, e) NC-$Al/Fe_2O_3(p)$ and (c, f) NC-$Al/Fe_2O_3(o)$.

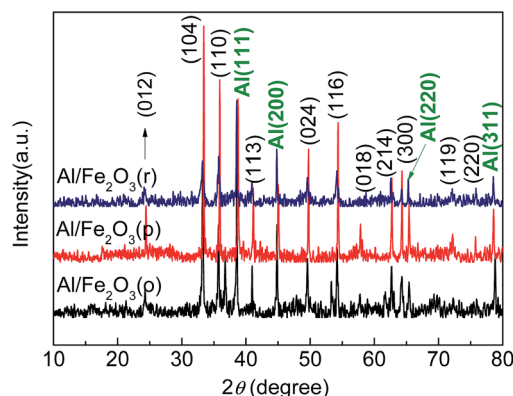**Fig. 2** SEM images of Al/Fe_2O_3. (a) $Al/Fe_2O_3(r)$; (b) $Al/Fe_2O_3(p)$ and (c) $Al/Fe_2O_3(o)$.

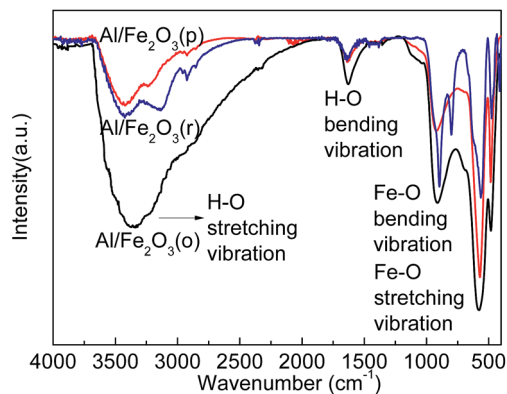**Fig. 4** XRD patterns of the Al/Fe_2O_3 superthermites.

Fig. 5 FT-IR spectra of the Al/Fe_2O_3 superthermites.

observed in the other two samples. These results indicate that there is no chemical reaction between n-Al and nano-Fe_2O_3.

The surface composition and chemical state of elements in Fe_2O_3 and the Al/Fe_2O_3 composites were further investigated *via* XPS. Fig. 6a shows the Fe and O elements of Fe_2O_3. In Fig. 6b, the wide scan XPS indicates the existence of Fe, O and Al elements in Al/Fe_2O_3. In Fig. 6c, two characteristic peaks are observed, which are ascribed to the Fe $2p_{1/2}$ and Fe $2p_{3/2}$ peaks. It can be seen that the Fe $2p_{1/2}$ peak is located at 724.7 eV (Fe_2O_3(o)), 724.5 eV (Fe_2O_3(p)) and 724.2 eV (Fe_2O_3(r)) and the Fe $2p_{3/2}$ peak is located at 711.0 eV (Fe_2O_3(o)), 710.9 eV (Fe_2O_3(p)) and 710.7 eV (Fe_2O_3(r)).[28,29] In the spectrum of Fe_2O_3(r), two accompanying satellite peaks are observed at 719.0 eV and

733.1 eV for Fe $2p_{3/2}$ and Fe $2p_{1/2}$, respectively, which indicate the existence of Fe^{3+}.[30,31] Similar satellite peaks can also be seen for Fe_2O_3(p) and Fe_2O_3(o). As illustrated in Fig. 6d, the peaks located at 724.8 eV, 724.5 eV, 724.9 eV and 711.1 eV, 711.2 eV, 711.6 eV are assigned to the Fe $2p_{1/2}$ and Fe $2p_{3/2}$, respectively, of Al/Fe_2O_3(o), Al/Fe_2O_3(p) and Al/Fe_2O_3(r).[32,33] The satellite peaks demonstrate that the chemical states of the Fe element remain constant, which further indicates the stability of the Al/Fe_2O_3 composites.

3.3 BET determination

Nitrogen adsorption/desorption isotherms were measured to determine the specific surface area and pore size distribution of the Fe_2O_3 nanostructures, and the corresponding images are presented in Fig. S1.† Fe_2O_3(p) exhibits a type H_3 hysteresis loop according to the IUPAC classification,[34] which indicates the presence of mesopores (2–50 nm). The pore size distribution of Fe_2O_3(p) indicates that it has mesoporous and microporous regions with a maximum peak pore diameter of 3.8 nm, as seen in Fig. S1.† The isotherms of Fe_2O_3(o) and Fe_2O_3(r) can be identified as type III, which indicates that the adsorbate–adsorbate interactions play an important role. The olivary Fe_2O_3 NPs exhibit a wide pore size distribution ranging from 1.4 to more than 30 nm which are mainly in the microporous and mesoporous region. The pore size of Fe_2O_3(r) is also microporous and mesoporous with a distribution primarily in the range of 1.4 to 32 nm. The Brunauer–Emmett–Teller (BET) specific surface areas of Fe_2O_3(p), Fe_2O_3(o), and Fe_2O_3(r) are 6.9, 3.1 and
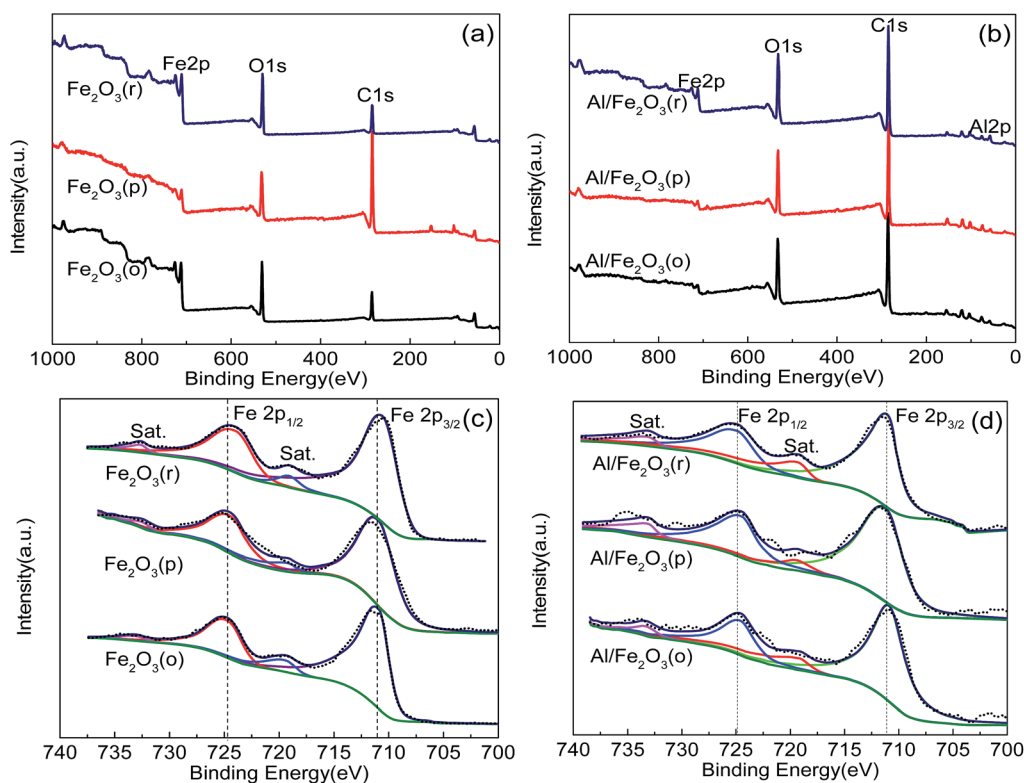

Fig. 6 XPS spectra for Fe_2O_3 and Al/Fe_2O_3. (a) Wide spectra of Fe_2O_3 and Al/Fe_2O_3 (b); (c) Fe 2p of Fe_2O_3; and (d) Fe 2p of Al/Fe_2O_3.

$37.5 \, \mathrm{m^2 \, g^{-1}}$, respectively. High-surface-area inorganic oxides have attracted much attention because they exhibit numerous edges and corners for adsorption and activation of reactions.[35,36] Especially, nanorods particles, as one-dimensional nano-structure materials, are of interest due to their peculiar properties, which originate from their high surface area, low dimensionality and dominant facets.[37–39]

3.4 Raman spectroscopy and laser ignition analysis

Fig. 7 shows the Raman spectra of the three Fe_2O_3 samples. Five optical phonon modes are observed for all three Fe_2O_3 nano-particle samples, which correspond to the A_g: 221 and 489 cm^{-1} and E_g: 288, 400 and 600 cm^{-1} vibrations.[40] The same peak positions show that these three samples are the same material, Fe_2O_3. However, the spectrum for $Fe_2O_3(p)$ is broader in line width, indicating larger crystal sizes or domains, which have a smaller surface-to-volume ratio and are thus less desirable for catalysis applications that require large surface areas.

In order to ascertain the activation of the three Fe_2O_3 samples, laser ignition analysis was also employed on a carbon dioxide laser ignition (SLC 110) system composed of four components: laser source, experimental container, high voltage impulse tester and test recorder. The maximum laser power is 120 W with a wavelength of 10.6 μm and the laser spot diameter on the sample surface is 5.0 mm. Figures of the initial and final spark taken from the video of the laser ignition process of the three particles are shown in Fig. S2,† in which the ignition of $Fe_2O_3(p)$ has a weaker spark than that of the other two samples. Furthermore, the laser response delay time on $Fe_2O_3(p)$, $Fe_2O_3(o)$, and $Fe_2O_3(r)$ are 107.3, 104.0, and 98.7 ms (taken from three experiments), respectively. Usually, the laser response delay time indicates the reaction activation of a material, and the shorter it is, the more active the material will be.[41]

Based on the analysis of surface area detection, Raman spectroscopy and laser ignition, the rod-like Fe_2O_3 with a larger specific surface area than the other two samples may have a more reactive activation on the Al/Fe_2O_3 catalyst in improving the thermal decomposition of NC.

3.5 Thermal analysis
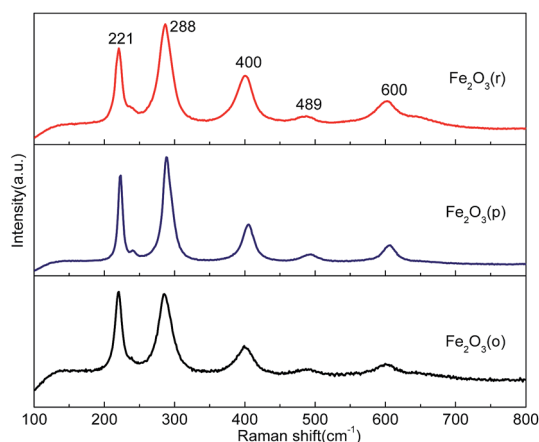
Fig. 8 shows the DSC heat flow curves of NC and the three different NC-Al/Fe_2O_3 composites at a heating rate of 10 °C min^{-1}. The peak temperatures of the decomposition process are given to evaluate the effects of Al/Fe_2O_3 on NC. The peak temperatures of NC, NC-$Al/Fe_2O_3(r)$, NC-$Al/Fe_2O_3(p)$ and NC-$Al/Fe_2O_3(o)$ are (209.83 ± 0.30), (209.43 ± 0.53), (209.48 ± 0.52) and (209.92 ± 0.31) °C, respectively. The decomposition peak temperatures of the NC-$Al/Fe_2O_3(r)$ and NC-$Al/Fe_2O_3(p)$ systems are almost equal, and they decompose at about 0.40 °C (calculated based on the data in Fig. 8) lower than NC alone. The decomposition peak temperature of NC-$Al/Fe_2O_3(o)$ is 209.92 °C, which is 0.09 °C higher than that of NC and 0.49 °C higher than that of NC-$Al/Fe_2O_3(r)$. Therefore, the three different shaped Al/Fe_2O_3 superthermites have an effect on NC at high temperature. To further study the role of Al/Fe_2O_3 in the NC-based composite energetic materials, the decomposition mechanism of NC and NC-Al/Fe_2O_3 were investigated.

3.6 Non-isothermal reaction kinetics

The thermal analysis shows that the decomposition temperature of NC-$Al/Fe_2O_3(r)$ is the lowest among the three obtained NC-based superthermite composites. To explore the reaction mechanism of the intense exothermic decomposition process of NC-$Al/Fe_2O_3(r)$ and obtain the corresponding kinetic parameters (E_a and A) and the most probable kinetic model functions, the DSC curves at the heating rates of 5.0, 10.0, 15.0, 20.0, 25.0 and 30.0 °C min^{-1} were processed mathematically. The temperature data corresponding to the conversion degrees (α) were found. Six integral methods (MacCallum–Tanner, Šatava–Šesták, Agrawal, General integral, Universal integral, and Flynn-Wall-Ozawa) and one differential method (Kissinger) were employed.[42–46] The values of E_a were obtained using Ozawa's method from the iso-conversional DSC curves at the six heating rates,[45,46] and the E_a–α relation is shown in Fig. 9. From Fig. 9, it can be seen that the activation energy slightly changes in the region of 0.175–0.675 (α), thus this range was selected to calculate the non-isothermal reaction kinetics.

Forty-one types of kinetic model functions and basic data were put into the integral and differential equations for the
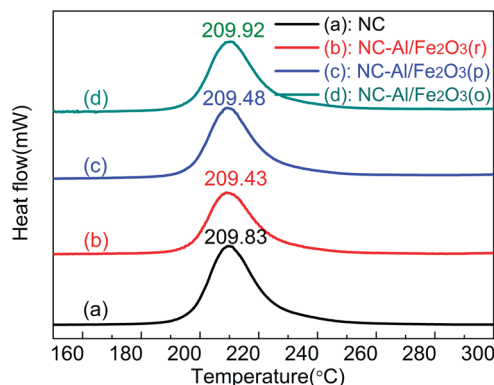

Fig. 7 Raman spectra of the different Fe_2O_3 samples.

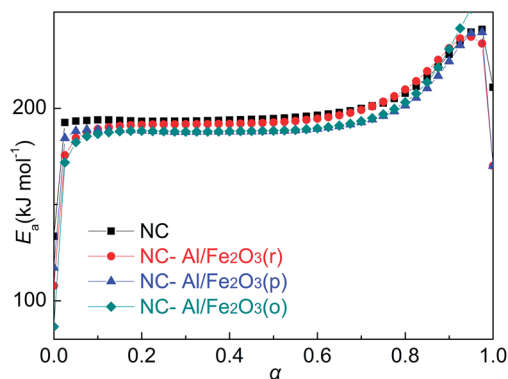**Fig. 8** DSC curves of NC-Al/Fe_2O_3 and NC.

Fig. 9 E_a *vs.* α curves of NC-Al/Fe$_2$O$_3$ and NC obtained from the Flynn-Wall-Ozawa method.

calculation.[47] The kinetic parameters and the probable kinetic model function were selected using the logical choice method which satisfied the ordinary range of the thermal decomposition kinetic parameters for energetic materials [E_a/(kJ mol^{-1}) = 80–250, log(A/s) = 7–30]. These data together with their appropriate values of linear correlation coefficient (r), standard mean square deviation (Q) and believable factor (d, where $d = (1 - r)$ Q), are presented in Table S1.†

The values of E_a and log A obtained from the single non-isothermal DSC curve is in good agreement with the calculated values obtained by Kissinger's method and Ozawa's method. Therefore, we conclude that the reaction mechanism for the intense exothermic decomposition process of NC-Al/Fe$_2$O$_3$(r) can be classified using the Avrami–Erofeev equation: $G(\alpha) = [-\ln(1 - \alpha)]^{2/3}$. Substituting $f(\alpha)$ with $1.5(1 - \alpha)[-\ln(1 - \alpha)]^{1/3}$, E_a with 182.53 kJ mol^{-1} and A with $10^{17.49}$ s^{-1} in eqn (1),

$$\mathrm{d}\alpha/\mathrm{d}T = \frac{A}{\beta}f(\alpha)\mathrm{e}^{-E/RT} \quad (1)$$

where, $f(\alpha)$ and $\mathrm{d}\alpha/\mathrm{d}T$ are the differential model function and the rate of conversion, respectively.

The kinetic equation of the exothermic decomposition reaction can be described as eqn (2),

$$\frac{\mathrm{d}\alpha}{\mathrm{d}T} = \frac{10^{17.67}}{\beta}(1 - \alpha)\left[-\ln(1 - \alpha)\right]^{1/3}\exp\left(-2.20 \times 10^4/T\right) \quad (2)$$

In order to check the constancy and validity of the apparent activation energy (E_a) obtained from the logical choice method, an integral isoconversional non-linear (NL-INT) method was applied to verify the E_a in the same range of α.[48–50] The values of $E_{\mathrm{NL\text{-}INT\text{-}SY3}}$ (SY3 means that the integral method $I(E_\alpha, T_{\alpha,i})$ in eqn (3) adopts the three order approximation of the Senum–Yang equation) were obtained by substituting the original data determined from DSC into eqn (3) and listed in Table S5.† The results show that the apparent activation energies calculated using these two methods are close to each other. The final mean value of apparent activation energy (E_a) is close to the mean value of $E_{\mathrm{NL\text{-}INT\text{-}SY3}}$, which further indicates that the kinetic model function and the values of E_a are reliable to a great extent.

Table 1 Calculated values of the kinetic parameters for NC and the three NC-Al/Fe$_2$O$_3$ composites

Sample	E_a/kJ mol^{-1}	log(A/s)	T_{be0}/°C
NC	207.48	20.22	191.42
NC-Al/Fe$_2$O$_3$(p)	191.75	18.51	190.25
NC-Al/Fe$_2$O$_3$(o)	186.18	17.87	189.39
NC-Al/Fe$_2$O$_3$(r)	182.53	17.49	187.50

$$\Omega_{1I}(E_\alpha) = \min\left|\sum_{i=1}^{n}\sum_{j \neq i}^{n}\frac{\beta_j \times I(E_\alpha, T_{\alpha,i})}{\beta_i \times I(E_\alpha, T_{\alpha,j})} - n(n-1)\right| \quad (3)$$

3.7 Thermal safety studies

The values (T_{e0} and T_{p0}) of the onset temperature (T_e) and peak temperature (T_p) corresponding to $\beta \to 0$ obtained from eqn (4) are 177.96 °C and 193.50 °C, respectively.

$$T_e = T_{\mathrm{e0}} + a\beta_i + b\beta_i^2 + c\beta_i^3, \; i = 1\text{–}6 \quad (4)$$

where, a, b and c are coefficients.

The thermal ignition temperature (T_{be0}) was obtained by substituting E_{eo} and T_{e0} into the eqn (5) by Zhang *et al.*,[51] and the value (T_{be0}) of 187.50 °C was obtained.

$$T_{\mathrm{be0(or\ bp0)}} = \frac{E_O - \sqrt{E_O{}^2 - 4E_O RT_{\mathrm{e0(or\ p0)}}}}{2R} \quad (5)$$

The thermal behaviors of NC-Al/Fe$_2$O$_3$(p), NC-Al/Fe$_2$O$_3$(o) and NC were also analyzed *via* the same method using the data in Fig. 8. The corresponding kinetic parameters are presented in Table S2–S4.† The results show that the reaction mechanism of their intense exothermic decomposition process is classified as reaction orders $f(\alpha) = 1.5(1 - \alpha)[-\ln(1 - \alpha)]^{1/3}$ and $G(\alpha) = [-\ln(1 - \alpha)]^{2/3}$. The calculated values of the kinetic parameters of the decomposition reaction for NC and the three NC-Al/Fe$_2$O$_3$ composites are listed in Table 1.

From the thermal analysis, the addition of Al/Fe$_2$O$_3$ does not change the kinetic model function of NC, but reduces the thermal ignition temperature (T_{be0}) and decreases the values of E_a and A. Among the three NC-Al/Fe$_2$O$_3$ composites, Al/Fe$_2$O$_3$(r) is the best since it possesses the lowest thermal ignition temperature, activation energy and frequency factor of NC and the Fe$_2$O$_3$(r) particles can have a significant influence on the catalytic actions of superthermites; thus Fe$_2$O$_3$(r) is the preferred material for the preparation of Al/Fe$_2$O$_3$.

4. Conclusion

In summary, we prepared three thermites with different morphological Fe$_2$O$_3$ and further studied their thermal decomposition effects on NC for the first time by analyzing their thermal behaviors. The kinetic model functions of NC and the three NC-Al/Fe$_2$O$_3$ samples are classified using the Avrami–Erofeev equation $f(\alpha) = 1.5(1 - \alpha)[-\ln(1 - \alpha)]^{1/3}$ in the

differential form. The ranking order of the values of the apparent activation energy (E_a) is as follows: NC-Al/Fe$_2$O$_3$(r) < NC-Al/Fe$_2$O$_3$(o) < NC-Al/Fe$_2$O$_3$(p) < NC. The thermal ignition temperature and frequency factor of NC-Al/Fe$_2$O$_3$(r) are the lowest. This is due to the fact that the Fe$_2$O$_3$ nanorod particles have the largest specific surface area, which could increase the interfacial contact points among the components. Therefore, the Al/Fe$_2$O$_3$(r) superthermite has substantial catalytic activity and the morphology of the Fe$_2$O$_3$ NPs helps to fabricate superthermites with excellent properties.

Acknowledgements

References

1 J. L. Cheng, H. H. Hng, Y. W. Lee, S. W. Du and N. N. Thadhani, *Combust. Flame*, 2010, **157**, 2241.

2 S. M. Begley and M. Q. Brewster, *J. Heat Transfer*, 2007, **129**, 624.

3 M. L. Pantoya and J. J. Granier, *Propellants, Explos., Pyrotech.*, 2005, **3**, 53.

4 J. J. Granier and M. L. Pantoya, *Combust. Flame*, 2004, **138**, 373.

5 L. L. Wang, Z. A. Munir and Y. M. Maximov, *J. Mater. Sci.*, 1993, **28**, 3693.

6 M. Petrantoni, C. Rossi, L. Salvagnac, V. Conédéra, A. Estève, C. Tenailleau, P. Alphonse and Y. J. Chabal, *J. Appl. Phys.*, 2010, **108**, 084323.

7 A. E. Stiegman, C. D. Park, M. Mileham, L. J. van de Burgt and M. P. Kramer, *Propellants, Explos., Pyrotech.*, 2009, **34**, 293.

8 K. S. Martirosyan, L. Wang, A. Vicent and D. Luss, *Nanotechnology*, 2009, **20**, 17579.

9 G. Q. Jian, N. W. Piekiel and M. R. Zachariah, *J. Phys. Chem. C*, 2012, **116**, 26881.

10 X. Zhou, M. Torabi, J. Lu, R. Shen and K. Zhang, *ACS Appl. Mater. Interfaces*, 2014, **6**, 3058.

11 N. N. Zhao, C. C. He, J. B. Liu, H. J. Gong, T. An, H. X. Xu, F. Q. Zhao, R. Z. Hu, H. X. Ma and J. Z. Zhang, *J. Solid State Chem.*, 2014, **219**, 67.

12 K. S. Martirosyan, L. Wang and D. Luss, *Chem. Phys. Lett.*, 2009, **483**, 107.

13 S. M. Umbrajkar, M. Schoenitz and E. L. Dreizin, *Propellants, Explos., Pyrotech.*, 2006, **31**, 382.

14 D. G. Xu, Y. Yang, H. Cheng, Y. Y. Li and K. L. Zhang, *Combust. Flame*, 2012, **159**, 2202.

15 T. Ulrich, *Energetic Materials: Particle Processing and Characterization*, Wiley-Vch Verlag GmbH & Co. KGaA, Weinheim, 2005, p. 245.

16 J. L. Cheng, H. H. Hng, H. Y. Ng, P. C. Soon and Y. W. Lee, *J. Phys. Chem. Solids*, 2010, **71**, 90.

17 S. Yan, G. Q. Jian and M. R. Zachariah, *ACS Appl. Mater. Interfaces*, 2012, **4**, 6432.

18 D. Zhang, X. Li, B. Qin, C. Lia and X. Guo, *Mater. Lett.*, 2014, **120**, 224.

19 S. He, J. Chen, G. Yang, Z. Qiao and J. Li, *Cent. Eur. J. Energ. Mater.*, 2015, **12**, 129.

20 K. B. Plantier, M. L. Pantoya and A. E. Gash, *Combust. Flame*, 2005, **140**, 299.

21 L. Qin, N. Yan, J. Li, H. Hao and F. Zhao, *RSC Adv.*, 2017, **7**, 7188.

22 M. A. Hassan, *J. Hazard. Mater.*, 2001, **88**, 33.

23 M. R. Sovizi, S. S. Hajimirsadeghi and B. Naderizadeh, *J. Hazard. Mater.*, 2009, **168**, 1134.

24 T. An, F. Q. Zhao, Q. Pei, L. B. Xiao, S. Y. Xu, H. X. Gao and X. L. Xing, *Chin. J. Inorg. Chem.*, 2011, **27**, 231.

25 R. Li, H. Xu, H. Hu, G. Yang, J. Wang and J. Shen, *J. Energ. Mater.*, 2014, **32**, 50.

26 Y. Yang, H. X. Ma, J. Zhuang and X. Wang, *Inorg. Chem.*, 2011, **50**, 10143.

27 H. Ren, Y. Y. Liu, Q. J. Jiao, X. F. Fu and T. T. Yang, *J. Phys. Chem. Solids*, 2010, **71**, 149.

28 N. S. Mcintyre and D. G. Zetaruk, *Anal. Chem.*, 1977, **49**, 1521.

29 C. Fu, A. Mahadevegowda and P. Grant, *J. Mater. Chem. A*, 2016, **4**, 2597.

30 S. Liu, K. Yao, L. H. Fu and M. G. Ma, *RSC Adv.*, 2016, **6**, 2135.

31 J. Balbuena, M. Cruz and A. L. Cuevas, *RSC Adv.*, 2016, **6**, 92917.

32 D. H. Taffa, I. Hamm, C. Dunkel, I. Sinev and D. Bahnemann, *RSC Adv.*, 2015, **5**, 1702.

33 T. Yamashita and P. Hayes, *Appl. Surf. Sci.*, 2008, **254**, 2441.

34 K. S. W. Sing, D. H. Everett, R. A. W. Haul, L. Moscou, R. A. Pierotti, J. Rouquerol and T. Siemieniewska, *Pure Appl. Chem.*, 1985, **57**, 603.

35 D. Terribile, A. Trovarelli, A. De Leitenburg and G. Dolcetti, *Chem. Mater.*, 1997, **9**, 2676.

36 M. Daturi, E. Finocchio, C. Binet, J. C. Lavalley, F. Fally, V. Perrichon, H. Vidal, N. Hickey and J. Kašpar, *J. Phys. Chem. B*, 2000, **104**, 9186.

37 Y. Xia, P. Yang, Y. Sun, Y. Wu, B. Mayers, B. Gates, Y. Yin, F. Kim and H. Yan, *Adv. Mater.*, 2003, **15**, 353.

38 K. Woo, H. J. Lee, J. P. Ahn and Y. S. Park, *Adv. Mater.*, 2003, **15**, 1761.

39 X. M. Zhou, J. Y. Lan, G. Liu, K. Deng, Y. L. Yang, G. J. Nie, J. G. Yu and L. J. Zhi, *Angew. Chem., Int. Ed.*, 2012, **51**, 178.

40 P. Lottici, C. Baratto, D. Bersani, G. Antonioli, A. Montenero and M. Guarneri, *Opt. Mater.*, 1998, **9**, 368.

41 T. An, F. Q. Zhao, H. X. Hao, H. X. Ma, E. G. Yao, Y. Yang and Y. Tan, *Chin. J. Explos. Propellants*, 2011, **34**, 67.

42 H. X. Ma, B. Yan, Y. H. Ren, Y. Hu, Y. L. Guan, F. Q. Zhao, J. R. Song and R. Z. Hu, *J. Therm. Anal. Calorim.*, 2011, **103**, 569.

43 H. X. Ma, B. Yan, J. F. Li, Y. H. Ren, Y. S. Chen, F. Q. Zhao, J. R. Song and R. Z. Hu, *J. Mol. Struct.*, 2010, **981**, 103.

44 H. X. Ma, B. Yan, Z. N. Li, Y. L. Guan, J. R. Song, K. Z. Xu and R. Z. Hu, *J. Hazard. Mater.*, 2009, **169**, 1068.

45 M. E. Brown, M. Maciejewski, S. Vyazovkin, R. Nomen, J. Sempere, A. Burnham, J. Opfermann, R. Strey,

H. L. Anderson, A. Kemmler, R. Keuleers, J. Janssens, H. O. Desseyn, C. R. Li, T. B. Tang, B. Roduit, J. Malek and T. Mitsuhashi, *Thermochim. Acta*, 2000, **355**, 125.

46 S. Vyazovkin, A. K. Burnham, J. M. Criado, L. A. Pérez-Maqueda, C. Popescud and N. Sbirrazzuoli, *Thermochim. Acta*, 2011, **520**, 1.

47 R. Z. Hu and Q. Z. Shi, *Thermal Analysis Kinetics*, Science Press, Beijing, 2001, p. 127.

48 S. Vyazovkin and D. Dollimore, *J. Chem. Inf. Comput. Sci.*, 1996, **36**, 42.

49 S. Vyazovkin, *J. Comput. Chem.*, 1997, **18**, 393.

50 S. Vyazovkin, *J. Comput. Chem.*, 2001, **22**, 178.

51 T. L. Zhang, R. Z. Hu, Y. Xie and F. P. Li, *Thermochim. Acta*, 1994, **244**, 171.